

Hard and bright gamma-ray emission at the base of the *Fermi* bubbles

L. Herold ^{*1} and D. Malyshev ^{**1}

Erlangen Centre for Astroparticle Physics, Erwin-Rommel-Str. 1, Erlangen, Germany

Received September 15, 1996; accepted March 16, 1997

ABSTRACT

Context. *Fermi* bubbles (FB) are one of the most unexpected discoveries in the *Fermi*-LAT data. Although the FB were discovered more than 7 years ago, the questions of the origin of the bubbles and of the nature of the gamma-ray emission are still unresolved. Understanding the behavior of the bubbles near the Galactic plane may give a key to resolve the question of the origin of the bubbles.

Aims. We analyze 8 years of the *Fermi* LAT pass 8 data to study the gamma-ray emission at the base of the FB.

Methods. We use several methods to separate the gamma-ray emission of the bubbles from the Galactic foreground diffuse emission and from point sources.

Results. The gamma-ray emission at the base of the FB is consistent with a single power-law up to 1 TeV energies and has higher intensity than the FB emission at high latitudes. This bright and hard component of the emission is shifted to the West (negative longitudes) from the GC. Although it is possible that the hard component of emission is located at a different distance along the line of sight relative to the FB, the similarity of the spectra at energies below 100 GeV and the spatial coincidence make it plausible that the hard component is related to the FB observed at high latitudes.

Key words. Gamma rays: general – Galaxy: center – Galaxy: halo – ISM: jets and outflows

Contents

1	Introduction
2	Data selection
3	Modeling of the <i>Fermi</i> bubbles at low latitudes
3.1	East – West asymmetry in the data
3.2	Low energy data as a background model
3.3	Rectangles model of the bubbles
3.4	GALPROP model of the foreground and PS refitting
4	Discussion
4.1	Profile plots
4.2	Comparison of the spectra at different latitudes
4.3	IC model of the gamma-ray emission
4.4	Hadronic model of gamma-ray emission
5	Conclusions
A	Appendix

1. Introduction

- 1 Discussion of the *Fermi* bubbles properties at high latitudes.
- 1 Discussion of the models of the bubbles. Motivate the study at low latitudes.
- 2 Discuss the previous results – hints for higher intensity and harder spectrum near the GP, also the asymmetry with respect to the GC.
- 2 Main goal of this paper - analysis of the *Fermi* bubbles within 10° from the GP. Especially at high energies.

2. Data selection

- 3 The main goal of the analysis is a study of a relatively small region $\lesssim 10^\circ$ from the GC for energies $\gtrsim 1$ GeV. We use 9 years of the *Fermi*-LAT Pass 8 Source class events between August 4, 2008 and August 3, 2017 (*Fermi* Mission Elapsed Time 239557418 s – 523411376 s) with energies between 316 MeV = $10^{2.5}$ MeV and 1 TeV separated in 21 logarithmic energy bins (6 bins per decade). The selection of the events
- 6 is performed with the standard quality cuts. In order to avoid contamination from gamma rays produced in interactions of cosmic ray in the Earth atmosphere, we select
- 8

* e-mail: laura.herold@fau.de

** e-mail: dmitry.malyshev@fau.de

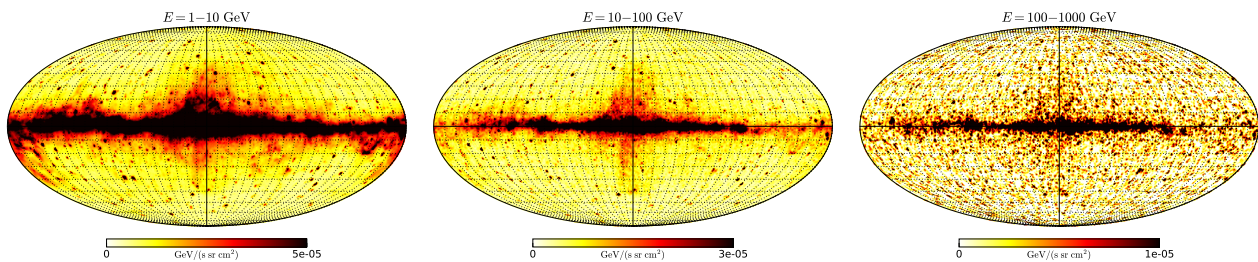


Fig. 1: 9-year *Fermi* data in three different energy ranges.

events with the zenith angles $\theta < 100^\circ$, which is sufficient for energies above 316 MeV. We calculate the exposure and PSF using the *Fermi*-LAT Science Tools package version 10-01-01 available from the *Fermi* Science Support Center¹ with the P8R2_SOURCE_V6 instrument response functions. For spatial binning we use HEALPix² (Górski et al. 2005) scheme with a pixelization of order 7 (≈ 0.46 pixel size).

3. Modeling of the *Fermi* bubbles at low latitudes

One of the main problems in the analysis of the FB near the GC is the presence of the foreground emission components, such as the interactions of cosmic rays with the interstellar gas and radiation fields. In order to test the possible effects of the foreground emission modeling, we use several methods to estimate the contribution of the foreground emission to the data.

In particular, there is a tentative displacement of the FB to the right of the GC, e.g., negative Galactic latitudes (Acero et al. 2016; Ackermann et al. 2017), with a spectrum that is harder than the spectrum of the FB at high latitudes (Ackermann et al. 2017). If we assume that the Galactic emission components are approximately symmetric with respect to the GC, then we can simply mask PS and calculate the difference in gamma-ray flux to the left and to the right from the GC. The difference should be approximately equal to the asymmetric part of the FB emission under the assumption that the other Galactic components and unresolved PS are symmetric with respect to the GC (Section 3.1).

In order to further test the hypothesis of the asymmetric and hard emission from the FB at low latitudes, we use the data at energies $\lesssim 1$ GeV to create a template of the Galactic emission, provided that the expected contribution of the FB at these energies is small relative to the rest of the Galactic components. Then we fit the template derived from the low energy data together with an isotropic template at higher energies outside of the FB area. The FB intensity is determined by extrapolating the model inside the FB area using the full template and by subtracting the

model from the data (Section 3.2). As an alternative approach, instead of fitting outside of the FB area, we add independent flat rectangular templates with the size approximately following the FB size to the model and fit over the whole sky. The flux attributed to these rectangular templates is used as an estimate of the average flux in the FB in the corresponding areas (Section 3.3).

We also calculate the flux attributed to the bubbles using one of the diffuse emission models from (Ackermann et al. 2017) (Section 3.4).

3.1. East – West asymmetry in the data

As a first simple check of the asymmetry at low latitudes, we compare the unprocessed *Fermi*-LAT data east and west of the Galactic center. After masking PS, we average the data over a region to the West (longitudes $0^\circ < \ell < 10^\circ$) and to the East ($-10^\circ < \ell < 0^\circ$) of the Galactic center for different latitudes. The regions have a latitude width of 10° for $b > |10^\circ|$ and a width of 4° for $b < |10^\circ|$. The difference of the averaged intensity of emission West minus East of the GC is shown in Fig. 2. At high latitudes, $b > |10^\circ|$, the emission is relatively symmetric. The emission for latitudes $b \in (-6^\circ, -2^\circ)$ and $b \in (-2^\circ, 2^\circ)$ shows excess emission to the West of the Galactic center, which remains significant at high energies.

3.2. Low energy data as a background model

Gamma rays produced in interactions of CR with gas and IC scattering dominate the gamma-ray emission around the GC in the energy range $E \lesssim 1$ GeV. Consequently, low-energy *Fermi*-LAT data is a good tracer for diffuse gamma-ray emission in the Galactic plane and can be used to create a spatial template for the Galactic foreground. The for the *Fermi*-LAT photons between 316 MeV and 1 GeV (averaged with E^{-2} spectrum) is about 1.5 , which is much worse than the sub-degree angular resolution above 1 GeV. In order to compensate for the difference in the angular resolution, we smooth the data in each high-energy bin with a Gaussian kernel of 1° (which corresponds to 68% containment angle of 1.5 in 2 dimensions).

¹ <http://fermi.gsfc.nasa.gov/ssc/data/analysis/>

² <http://sourceforge.net/projects/healpix/>

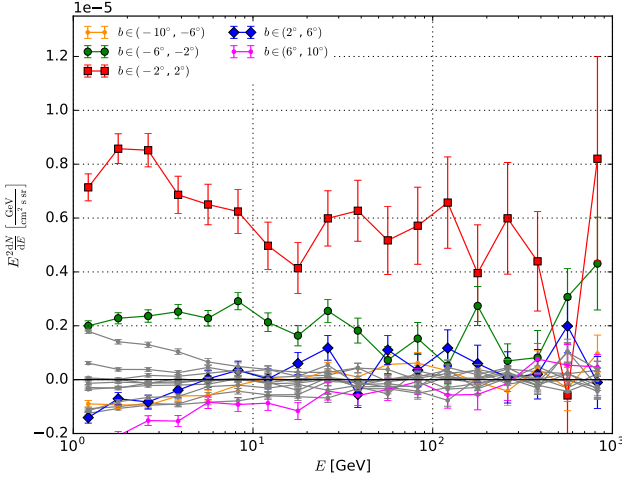


Fig. 2: Difference West minus East in the *Fermi*-LAT intensity relative to the GC after masking bright point sources. The mask is made symmetric using point reflection relative to the GC. The West (East) region has $-10^\circ < \ell < 0^\circ$ ($0^\circ < \ell < 10^\circ$).

We cut the sky horizontally in latitude stripes with the width of 4° and define our model in each stripe and energy bin separately. In the latitude stripe ℓ and energy bin E our model consists of a term proportional to the low-energy photon counts $k_{\ell\alpha} \cdot \tilde{N}_\ell^{\text{low}}(E, x)$, summed over all energies in 0.3 - 1.0 GeV, and an additional term $c_\ell(E) \cdot \tau(x, E)$ proportional to exposure $\tau(x, E)$:

$$N_\ell^{\text{model}}(E, x) = k_\ell(E) \cdot \tilde{N}_\ell^{\text{low}}(E, x) + c_\ell(E) \cdot \tau(x, E). \quad (1)$$

The term proportional to the exposure takes into account the isotropic extragalactic background and partially compensates for the latitude dependent IC emission. To include the dependence of exposure on energy and position in the sky, the low-energy data is weighted by the ratio of exposure in the low and in the high energy bins in each pixel x :

$$\tilde{N}_\ell^{\text{model}}(E, x) = \frac{1}{n_{\text{low}}} \left(\sum_{\epsilon \in (0.3-1.0 \text{ GeV})} \frac{N_\ell^{\text{low}}(\epsilon, x)}{\tau(\epsilon, x)} \right) \cdot \tau(E, x), \quad (2)$$

where $n_{\text{low}} = 3$ is the number of low-energy bins between 316 MeV and 1 GeV.

We determine the parameters $c_\ell(E)$ and $k_\ell(E)$ by fitting the model to the *Fermi*-LAT data in energy bins $E > 1.0$ GeV using Poisson likelihood (with Python iminuit minimizer). Since we smooth the data before the fit, the Poisson log-likelihood is an approximation in this case. In order to avoid an overcompensation of the *Fermi* bubbles, the region $-20^\circ < \ell < 20^\circ$ is excluded from the fit. We mask the 200 brightest 3FGL PS with a circle of ra-

dius $\frac{\delta}{\sqrt{2}} + 1^\circ$ where $\delta = 0.46^\circ$ is the characteristic size of the pixels. We also symmetrize the PS relative to the GC in order to avoid possible bias by masking more pixels on one side of the GC. **Dima: do we symmetrize the PS mask in the analysis as well, not only in the calculation of the asymmetry in the data?**

After we fit the model in each latitude stripe, we interpolate it inside the bubbles ROI and find the residual by subtracting it from the data. Figure 3 shows the residual maps for three different energy ranges. The FB are clearly visible in the first two energy ranges, $E = 1 - 10$ GeV and $E = 10 - 100$ GeV, for $E = 100$ GeV – 1 TeV the statistics is low, but one can still see an excess near the GP.

3.3. Rectangles model of the bubbles

Our first simple ansatz for a model of the FB consists of rectangular templates that approximately cover the area of the FB. As a model for the foreground we again use the low-energy model from Section 3.2. As before, the fit is performed independently in each 4° latitude stripe. To explore the east-west asymmetry of the FB, two rectangular templates, one east ($-20^\circ - 0^\circ$) and one west ($0^\circ - 20^\circ$), are added to the low-energy model in each latitude stripe ℓ and energy bin E :

$$N_\ell^{\text{model}}(E, x) = k_\ell(E) \cdot \tilde{N}_\ell^{\text{low}}(E, x) + \tilde{c}_\ell(E, x) + R_\ell^{\text{east}}(E) + R_\ell^{\text{west}}(E). \quad (3)$$

We determine the normalization of the rectangles $R_\ell^{\text{east}}(E)$ and $R_\ell^{\text{west}}(E)$ and the parameters $k_\ell(E)$ and $c_\ell(E)$ by fitting the model to the *Fermi*-LAT data in energy bins $E > 1.0$ GeV. The resulting residual, shown in Fig. 4 for $E = 10 - 100$ GeV, is very similar to the low-energy model.

3.4. GALPROP model of the foreground and PS refitting

4. Discussion

4.1. Profile plots

Figure 6 shows the latitude profiles of the different models in differential flux. The flux increases towards the Galactic plane. Left-right asymmetry close to the Galactic center.

4.2. Comparison of the spectra at different latitudes

Figure 7 shows a comparison of the SED of the raw data (without point sources) and the three different models in a very thin latitude stripe covering the Galactic plane. The grey triangles show the difference in the raw data west minus east. All models give similar results.

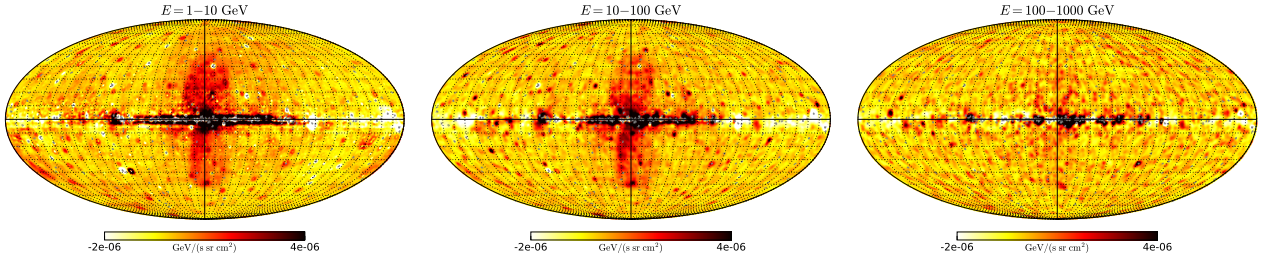


Fig. 3: Residuals of the low-energy model for three different energy ranges. The *Fermi* bubbles are clearly visible in the first two energy ranges. Point sources are masked.

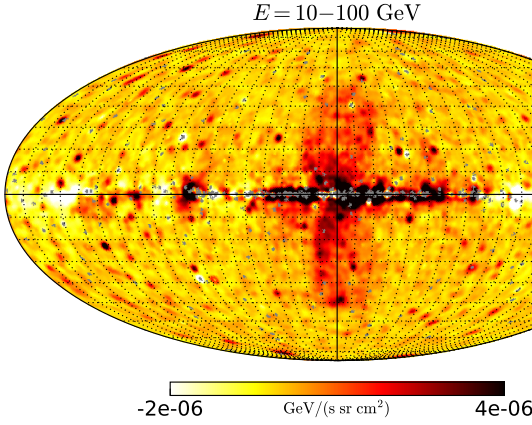


Fig. 4: Rectangles-model residual.

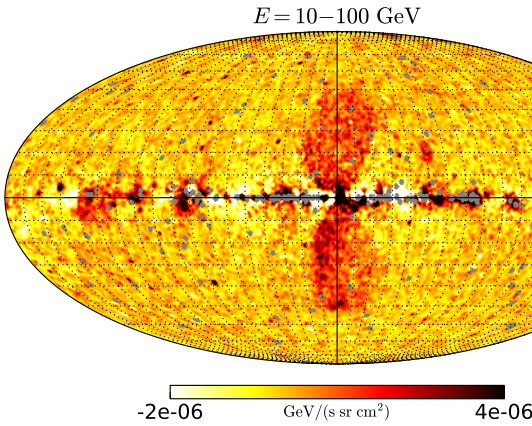


Fig. 5: GALPROP-model residuals in three different energy ranges.

To compare the behavior of the energy spectra at high energies for different latitudes, we fit a log-parabola

$$f(E) = N_0 E^{-\alpha - \beta \ln(E)} \quad (4)$$

in each latitude stripe. The local “index” of the spectrum at energy E is

$$n \equiv \frac{d \ln f}{d \ln E} = -\alpha - 2\beta \ln(E). \quad (5)$$

In Figure (???) we show a comparison of the SED index ($2-n$) for the bubbles spectra in different models at $E = 500$ GeV. For positive longitudes the index is relatively soft ($n < -2$) for most of the latitudes, except high latitudes where the gamma-ray statistics is small. For negative longitudes the index is near the GC is ≈ -2 , which is significantly harder than the index at higher latitudes.

4.3. IC model of the gamma-ray emission

IC radiation is produced in scattering processes of relativistic electrons on photons of the ISRF. The spectrum of the IC gamma radiation depends on the density of ISRF photons, the density of electrons and the differential Klein-Nishina cross section $d\sigma_{IC}/dE_\gamma$, taken from (Blumenthal & Gould 1970):

$$\left(\frac{dn}{dE}\right)_{\gamma, IC} = \iint \left(\frac{dn}{dE}\right)_{ISRF} \frac{d\sigma_{IC}}{dE_\gamma} \left(\frac{dn}{dE}\right)_e dE_{ISRF} dE_e. \quad (6)$$

The ISRF has three main components: starlight, IR and CMB. The IR and the starlight components are taken from the on-line distribution of GALPROP. For the CMB, we use the thermal spectrum with the temperature 2.73 K. We assume that the distribution of electrons follows a simple powerlaw and determine the normalization n_e and spectral index γ_e by fitting the IC spectrum(6) to the diffuse *Fermi* data using Poisson likelihood. Point sources are masked as described in Section 3.

Figure 8 shows the residual spectrum in the low-energy model within the latitude stripes $b \in (-2^\circ, 2^\circ)$ and $b \in (-6^\circ, -2^\circ)$. The dotted line represents the best-fit IC spectrum for an electron distribution following a simple powerlaw.

For the latitude stripe covering the Galactic plane, $b \in (-2^\circ, 2^\circ)$, adding a cutoff to the powerlaw does not improve the χ^2 -value at negative longitudes (blue, $\chi^2 = 715.4$ in both cases). For positive longitudes both a simple powerlaw and a powerlaw with a cutoff have similarly high χ^2 -values due to the large oversubtractions. For negative longitudes we find a lower bound for the cutoff energy at 14.9 TeV, for positive longitudes at 16.1 GeV, at

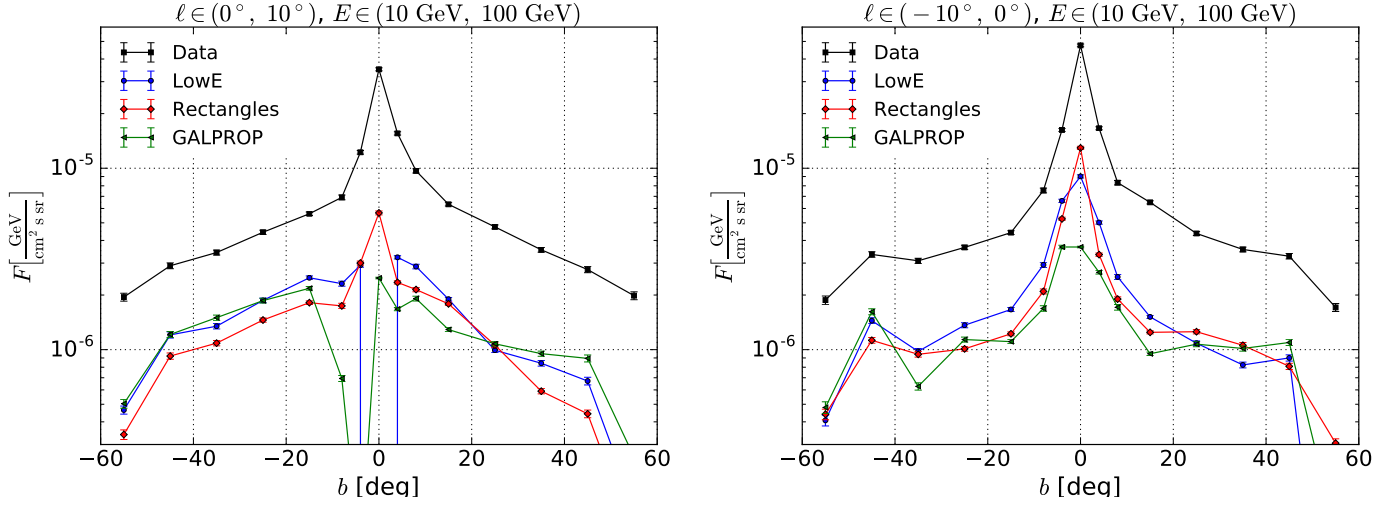


Fig. 6: Latitude profiles of the different models.

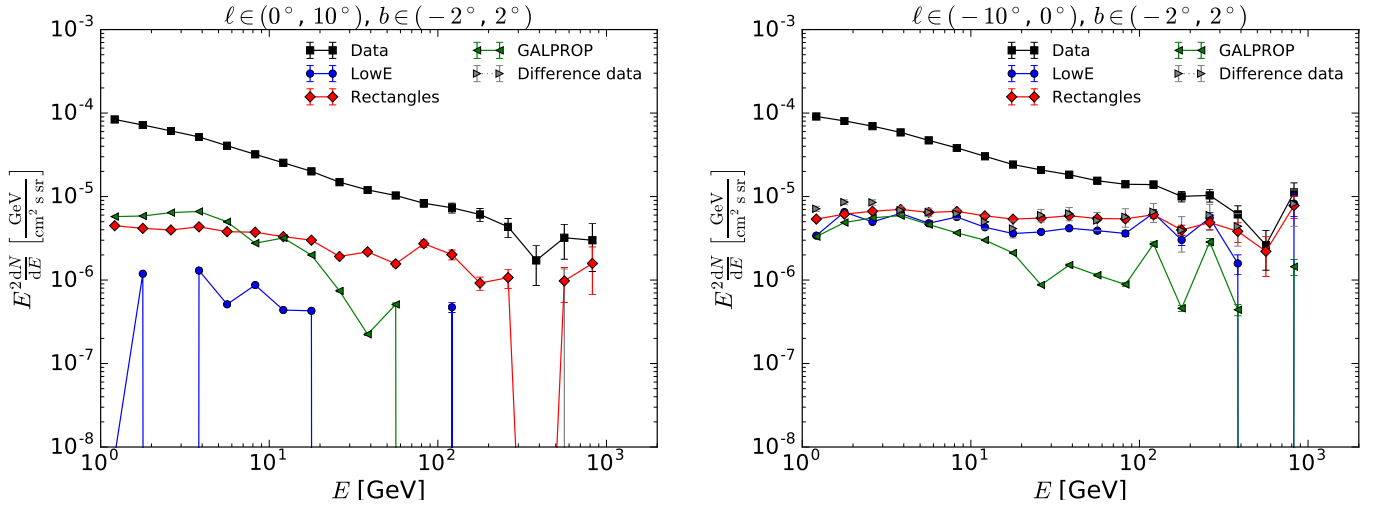


Fig. 7: Comparison of SED of all models.

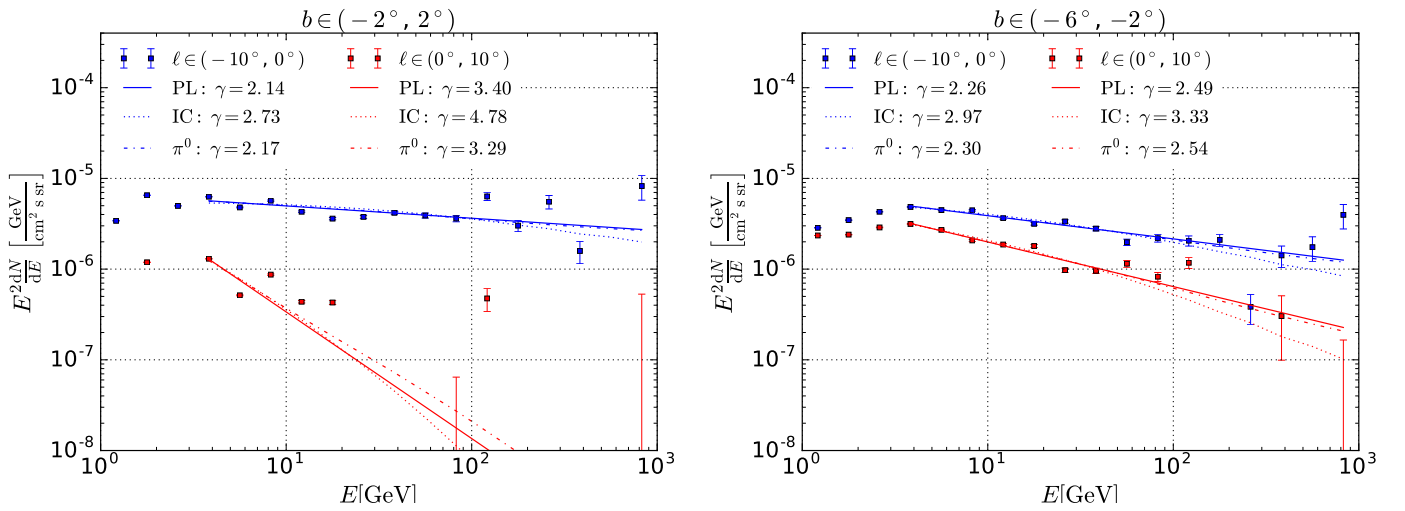


Fig. 8: SED of low-energy model with powerlaw and particle spectra fits.

a 95 %-confidence level.

Slightly below the Galactic plane, $b \in (-6^\circ, -2^\circ)$, the χ^2 -value does not improve by adding a powerlaw, neither at negative longitudes ($\chi^2 = 98.6$ in both cases) nor at positive longitudes ($\chi^2 = 155$ in both cases). For negative longitudes we find a lower bound for the cutoff energy at 22.0 TeV, for positive longitudes at 790.0 GeV, at a 95 %-confidence level.

Dima: we should first show here the fit with a simple power law (no cutoff) and then find the difference in χ^2 for the models with and without the cutoff. In the model with a cutoff, we should use the errors on the cutoff to determine 95% lower confidence limit on the cutoff value.

4.4. Hadronic model of gamma-ray emission

In the hadronic model, the gamma rays are produced as a result of collisions of hadronic CR with the interstellar gas. The spectrum of the gamma radiation depends on the density of interstellar gas n_H , the energy density of CR protons and the cross section to produce gamma rays in a proton-nucleus collisions:

$$\left(\frac{dn}{dE dt} \right)_{\gamma, \pi^0} = \int n_H \frac{d\sigma_p}{dE_\gamma} v_p \left(\frac{dn}{dT} \right)_p dT_p. \quad (7)$$

...

5. Conclusions

We want to estimate the properties that particles need to have to emit the gamma radiation observed in the region $b \in (-2^\circ, 2^\circ)$, $\ell \in (-10^\circ, 0^\circ)$. Averaged over the ROI, the best-fit spectrum of the electrons shows no cutoff and we conclude, that electrons of at least $E_0 = 1$ TeV need to be able to travel inside the whole volume of the ROI. We start with a diffusion equation taking into account diffusion and energy loss $b_{IC}(E)$ via IC. From the solution we read off the diffusion distance for electrons with energy $E_0 = 1$ TeV:

$$\langle x \rangle^2 = 2 \int_{E_0}^{\infty} \frac{D(E)}{b_{IC}(E)} dE = 1300 \text{ pc}. \quad (8)$$

We assumed a spatially constant diffusion coefficient $D(E) = D_0 \left(\frac{E}{1 \text{ GeV}} \right)^\delta$ with values of the local diffusion coefficient $D_0 = 3 \times 10^{28} \text{ cm}^2/\text{s} = 100 \text{ pc}^2/\text{kyr}$ and $\delta = 0.4$. The energy loss $b_{IC}(E)$ is ...

Assuming a distance of 8 kpc to the ROI, we find a height of 0.56 kpc in latitude and a length of 0.98 kpc in longitude. Since the diffusion distance of the electrons exceeds the spatial size of the ROI, the electrons cannot be confined. Therefore, we find that a transient process is favoured. The energy losses of protons exceed the energy losses of elec-

trons by far, therefore the same applies for protons.

With the local diffusion coefficient we find an escape time for both electrons and protons of

$$T = \frac{\Delta x^2}{2D(E)} = 70 \text{ kyr}. \quad (9)$$

The total energy density in electrons with energy above $E_0 = 1 \text{ GeV}$, which needs to be generated by this transient process, is given by the integral of the electron spectrum that was found in Section 4.3:

$$\frac{dE_{\text{tot}}}{dV} = \int_{E_0}^{\infty} \left(E \frac{dN}{dE} \right)_e dE = 4.9 \text{ meV/cm}^3. \quad (10)$$

Assuming that the depth along the optical axis coincides with the length in longitude, the volume of the ROI is $V = 0.54 \text{ kpc}^3 = 1.58 \times 10^{64} \text{ cm}^3$. The total energy content of the ROI in electrons above 1 GeV is $E_{\text{tot}} = 8 \times 10^{61} \text{ eV} = 1 \times 10^{50} \text{ erg}$, which corresponds to the CR energy output of 10 SNe.

Using the result from Section 4.4 we find an energy density in protons of $dE_{\text{tot}}/dV = 84 \text{ meV/cm}^3$ and a total energy content of $E_{\text{tot}} = 1 \times 10^{63} \text{ eV} = 2 \times 10^{51} \text{ erg}$. However, the gas density in the inner Galaxy is probably higher than $n_{\text{H}} = 1/\text{cm}^3$ as assumed in Section 4.4, resulting in an energy content in protons of the same order of magnitude as the energy density in electrons.

References

- Acero, F., Ackermann, M., Ajello, M., et al. 2016, *ApJS*, 223, 26
Ackermann, M., Ajello, M., Albert, A., et al. 2017, *ApJ*, 840, 43
Blumenthal, G. R. & Gould, R. J. 1970, *Reviews of Modern Physics*, 42, 237
Górski, K. M., Hivon, E., Banday, A. J., et al. 2005, *ApJ*, 622, 759

Appendix A: Appendix

If we need one.